

# Parity-Time-Symmetric Optical Lattice with Alternating Gain and Loss Atomic Configurations

Zhaoyang Zhang, Liu Yang, Jingliang Feng, Jiteng Sheng, Yiqi Zhang, Yanpeng Zhang,\* and Min Xiao\*

Since the periodic parity-time (PT)-symmetric potential can possess unique properties compared to a single PT cell (with only two coupled components), various schemes have been proposed to realize PT symmetry in optical lattices. Here, a PT-symmetric optical lattice is experimentally constructed with simultaneous gain and loss in an atomic medium. The gain and loss arrays are created in the four-level  $N$ -type configurations excited by spatially alternating strong and weak pump fields, respectively, which do not require discrete diffractions and can be realized more easily with more relaxed operating conditions. Also, the gain and loss coefficients can be modified independently. The dynamical behaviors of the system are investigated by measuring the phase difference between two adjacent gain and loss channels. The demonstrated PT-symmetric lattice with easy accessibility and better tunability shows obvious advantages in exploiting more peculiar properties and great improvements in practical applications of periodic PT-symmetric potentials.

manners, respectively. The experimental demonstrations of exact PT symmetry have been made most in pairs of coupled optical components (such as microresonators and waveguides) with respective gain and loss.<sup>[5]</sup> Given that a single PT cell (one pair of gain–loss elements) can exhibit many unconventional optical properties,<sup>[6–13]</sup> interesting, exotic features are expected in non-Hermitian optical lattices.<sup>[14–33]</sup> The proposed behaviors for light travelling through non-Hermitian lattices include non-Hermitian optical solitons,<sup>[15,16]</sup> non-Hermitian Bloch oscillation,<sup>[17,18]</sup> unidirectional invisibility,<sup>[20]</sup> and PT-symmetric Talbot effect.<sup>[25]</sup> Studying these novel effects in periodic non-Hermitian optical settings may provide new routes for exploring useful

## 1. Introduction


The studies on non-Hermitian Hamiltonians with entirely real eigenvalue spectra have advanced significantly in the past decade after the concept of parity-time (PT) symmetry<sup>[1,2]</sup> was introduced into optics, due to the formal equivalence between the Schrödinger equation in quantum mechanics and the paraxial wave propagation equation in optics.<sup>[3,4]</sup> Such equivalence causes the complex PT-symmetric potential to be easily realized in an optical setting by spatially arranging the real and imaginary components of the refractive index in even and odd symmetric

applications in non-Hermitian synthetic materials and further constructing on-chip optical integrated devices.

So far, experimental realizations of periodically arranged PT-symmetric potentials have been limited only to a few optical settings, such as a time-domain lattice realized in a network of coupled gain/loss fiber loops,<sup>[18,21]</sup> and an optical waveguide array with a lossy (without gain) background.<sup>[22]</sup> The known exact PT-symmetric optical lattice with spatially periodic gain and loss channels was realized in a four-level  $N$ -type atomic configuration.<sup>[34]</sup> In that experiment, two pairs of laser beams (coupling and pump fields) form the lattice with alternative

Dr. Z. Zhang, Prof. Y. Zhang, Prof. Y. Zhang  
Key Laboratory for Physical Electronics  
and Devices of the Ministry of Education  
& Shaanxi Key Lab of Information Photonic Technique  
School of Electronic and Information Engineering  
Xi'an Jiaotong University  
Xi'an 710049, China  
E-mail: ypzhang@mail.xjtu.edu.cn  
Dr. Z. Zhang, J. Feng, Prof. M. Xiao  
Department of Physics  
University of Arkansas  
Fayetteville, AR 72701, USA  
E-mail: mxiao@uark.edu

Dr. L. Yang  
College of Automation  
Harbin Engineering University  
Heilongjiang 150001, China  
Prof. J. Sheng  
State Key Laboratory of Precision Spectroscopy  
East China Normal University  
Shanghai 200062, China  
Prof. M. Xiao  
National Laboratory of Solid State Microstructures  
School of Physics  
Nanjing University  
Nanjing 210093, China

 The ORCID identification number(s) for the author(s) of this article can be found under <https://doi.org/10.1002/lpor.201800155>

DOI: 10.1002/lpor.201800155

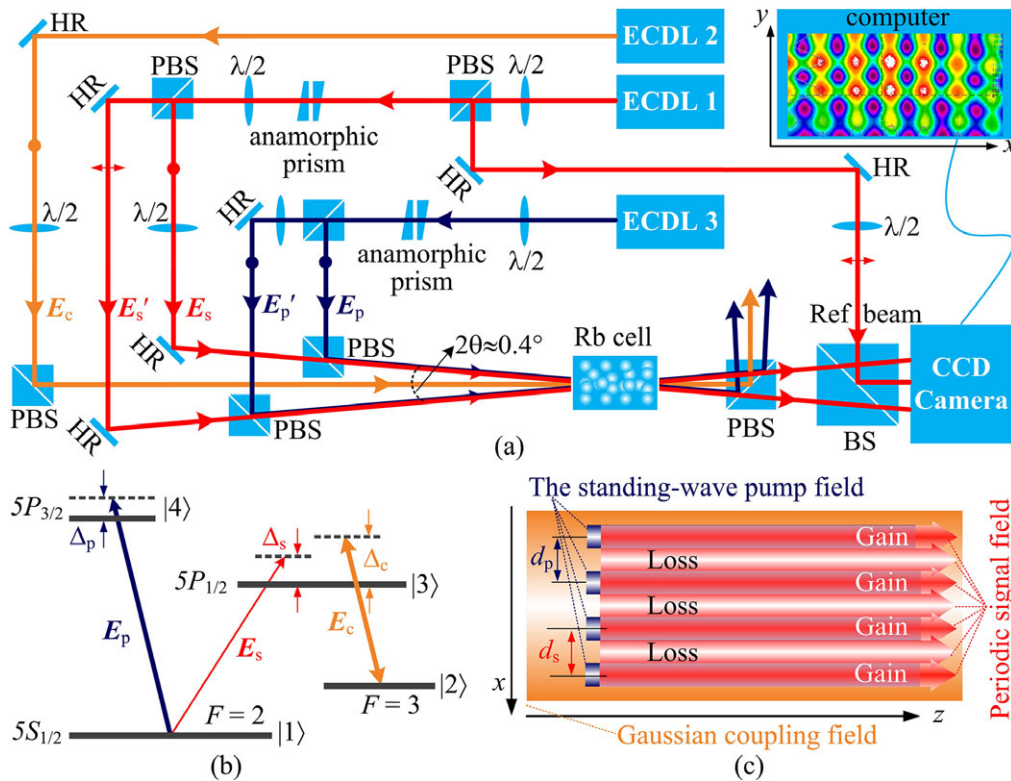


**Figure 1.** a) Experimental setup. The gain–loss modulated signal field and the phase information are detected by a CCD camera.  $E'_s$  and  $E_s$  are signal beams from the same laser EC DL1 and the pump beams  $E'_p$  and  $E_p$  are from EC DL3. The four laser beams ( $E_s$ ,  $E'_s$ ,  $E_p$ , and  $E'_p$ ) are shaped as ellipses with approximate axial diameters of 1.5 and 4.5 mm, respectively, by two pairs of anamorphic prisms. Although the two signal beams separate out of the cell in the schematic diagram, the two beams actually keep the interference pattern for a long distance even out of the cell. The reference beam intersects with the standing-wave signal field to generate the reference interference along the  $y$  direction. The double-headed arrow represents the horizontal polarization of a beam while the dot represents the vertical one. CCD, charge coupled device; EC DL, external cavity diode laser;  $\lambda/2$ , half-wave plate; HR, high-reflectivity mirror; PBS, polarization beam splitter. b) The four-level  $N$ -type energy-level configuration. c) The spatial arrangement of the laser fields inside the medium. The symbol  $z$  represents the propagation direction of light.

gain/loss channels in the atomic medium, and a Gaussian signal beam travelling through the medium experiences discrete diffractions from this spatially modulated PT-symmetric lattice. Such observation in solid materials is not easy to do due to various restrictions in material properties including the limitation on engineering desired periodic gain in certain materials as well as the connection between the real and imaginary parts of the index as imposed by Kramers–Kronig relations.<sup>[35]</sup> Different from solid-state systems, atomic media are quite easy and efficient in constructing desired real/imaginary refractive index profiles.<sup>[36,37]</sup> By making use of the laser-induced atomic coherence, particularly with the electromagnetically induced transparency (EIT)<sup>[38,39]</sup> technique, one can easily construct controllable and desired linear (dispersion, gain/loss) and nonlinear properties in coherently prepared multi-level atomic media.<sup>[40,41]</sup>

In this article, we experimentally demonstrate a new scheme to construct a spatially extended PT-symmetric optical lattice based on the periodical gain and loss channels induced in the four-level  $N$ -type atomic configuration driven with respective strong and weak pump fields, which appear alternately along the transverse  $x$  direction in the  $^{85}\text{Rb}$  atomic medium. The four-level  $N$ -type system is driven by a signal field ( $E_s$ ), a coupling field ( $E_c$ ), and a pump field ( $E_p$ ), as shown in **Figure 1b**. The strong

pump field can introduce Raman gain on the signal field while the weak pump field provides a modifiable loss under the EIT condition. With the intensity of the pump field set to zero, the four-level system even reduces down to a three-level one. The alternative strong and weak pump fields are achieved by injecting two pump beams with a small angle to establish a standing wave in the transverse ( $x$ ) direction. The pump-field intensity has its maximum and minimum (basically zero) at the interference peak and valley, respectively. When the coupling beam is sent in with an extended uniform (Gaussian) profile and two signal beams are injected in the same directions as the two pump beams, the detected signal-field profile exhibits interference pattern with the peak experiencing gain due to the four-level Raman gain process and the valley experiencing loss due to three-level EIT (with the weak pump field). This scheme is quite different from the one adopted in our previous work,<sup>[34]</sup> and consequently requires a distinct laser configuration. In the current work, the refractive index along the  $x$  direction can be spatially engineered in a periodic way with the assistance of an EIT window generated by the co-propagating standing-wave signal field (formed by two signal beams with different intensities) and Gaussian coupling field. Based on this periodic EIT configuration, with the standing-wave pump field turned on and adjusted

to completely overlap with the signal field, gain and loss can be effectively generated at the bright and dark fringes of the signal field, respectively. Such periodic gain–loss pairs can be exploited to construct a spatially distributed PT-symmetric optical lattice by appropriately tuning the gain/loss ratio, which can be easily manipulated by adjusting the pertinent parameters including the atomic density, the periodicity of the standing waves, the frequency detunings, and Rabi frequencies of corresponding fields.

One of the key advantages of the current system is that the parameters responsible for the gain and loss in different channels can now be modified separately, so it is easier to control the gain/loss ratio. To be specific, the signal and pump lattices are completely overlapped and one can modify only the gain (loss) coefficient by setting proper intensity for the bright (dark) fringe of the lattices. Also, the coupling strength can be changed without affecting the gain/loss ratio by slightly adjusting the angles between the beams for inducing the lattices. Consequently, the current system is easy accessible and provides better tunability. To demonstrate the characteristic features of the system, we measure the relative phase difference between two adjacent gain/loss channels by utilizing a reference beam to interfere with the signal field (along the  $y$  direction). All the experimental observations can be explained by the numerical simulations.

## 2. Experimental Section

The experimental scheme is shown in Figure 1a. The standing-wave signal field and the other laser fields (standing-wave pump field and large-size Gaussian coupling field) propagate along the same  $z$  direction to establish this periodical alternating gain and loss atomic configurations. The  $N$ -type four-level  $^{85}\text{Rb}$  atomic energy-level structure (see Figure 1b), consisting of two hyperfine states  $F = 2$  (level  $|1\rangle$ ) and  $F = 3$  ( $|2\rangle$ ) of the ground state  $5S_{1/2}$  and two excited states  $5P_{1/2}$  ( $|3\rangle$ ) and  $5P_{3/2}$  ( $|4\rangle$ ), can provide gain or loss under different parametric regimes.

To be specific, two elliptically shaped signal beams  $E_s$  and  $E'_s$  (wavelength  $\lambda_c = 794.97$  nm, frequency  $\omega_s$ , Rabi frequencies  $\Omega_s$ , and  $\Omega'_s$  [ $\Omega_s \neq \Omega'_s$ ], respectively) from the same external cavity diode laser (ECDL1) are symmetrically arranged with respect to the  $z$  axis and intersect at the center of the rubidium cell with an angle of  $2\theta \approx 0.4^\circ$  to establish a periodical signal field in the  $x$  direction. Due to intensity difference between the two signal beams, the intensity of the interference valley is not zero. The 7.5 cm long cell is wrapped with  $\mu$ -metal sheets to shield the magnetic field and heated to 75 °C by the heat tape. The small-angle arrangement can make the signal beam maintain a standing-wave field for a relatively long distance (over 20 cm) along the  $z$  direction. With the frequency of the strong Gaussian coupling beam  $E_c$  ( $\lambda_c = 794.97$  nm,  $\omega_c$ ,  $\Omega_c$ ) tuned to be near resonant with the transition  $|2\rangle \leftrightarrow |3\rangle$ , a  $\Lambda$ -type EIT configuration is achieved in the  $|1\rangle \leftrightarrow |2\rangle \leftrightarrow |3\rangle$  subsystem. As the coupling beam is large enough to cover the entire standing-wave signal field, the spatially periodic EIT (along the  $x$  direction) can be observed at the output surface of the cell. Namely, both the bright and dark fringes on the signal field experience certain losses (with different signal-field intensities). Next, the two pump beams  $E_p$  and

$E'_p$  ( $\lambda_p = 780.24$  nm,  $\omega_p$ ,  $\Omega_p$  and  $\Omega'_p$ , respectively) are incident into the cell with almost the same angle of  $2\theta \approx 0.4^\circ$  to build the periodical pump field with  $\Omega_p = \Omega'_p$ , that is, the intensity of the interference valley point is nearly zero. The presence of the standing-wave pump field with proper intensity can introduce an alternating Raman gain on the signal field under the four-level  $N$ -type configuration.<sup>[42]</sup> The schematic diagram for the spatial arrangement of the three fields inside the cell is shown as Figure 1c, where the signal-field array completely overlaps with the pump-field array. The gain is generated when the pump field is strong enough (corresponding to the configuration in the bright fringes) while the signal experiences loss with a weak pump field (corresponding to the configuration in the dark fringes). Since the signal field has orthogonal polarization from the pump and coupling fields, we can reject the pump and coupling fields with a polarization beam splitter and monitor only the signal field on a charge coupled device (CCD) camera.

With the gain–loss modulated periodic signal field obtained, we introduce a reference beam (from the same ECDL1 as  $E_s$ ) to interfere with the signal beam and determine the relative phase difference (representing the internal phase difference of the eigenvectors in the system) between the adjacent gain and loss channels. Here the reference beam is coupled into the signal light path via a 50/50 beam splitter along the  $y$  direction (see Figure 1a). Both the output signal beam and the phase information are monitored by the CCD camera.

## 3. Theory

Theoretically, the signal field and the coupling field can drive a three-level EIT configuration to modulate the refractive index for the signal field. In the presence of the intensity-modulated (periodic) pump field, the imaginary part of the index as seen by the signal field can be alternately above (absorption/loss) and below (gain) zero along  $x$ . In detail, based on the density-matrix equations for the four-level atomic configuration,<sup>[31]</sup> the susceptibility for describing the optical response of the signal field can be obtained through the expression  $\chi = (2N\mu_{13}/\epsilon_0 E_s) \times \rho_{31}$ . Here  $\rho_{31}$  is the density-matrix element for the transition  $|1\rangle \leftrightarrow |3\rangle$ ;  $N$  is the atomic density;  $\mu_{ij}$  ( $i, j = 1, 2, 3, 4$ ) is the dipole moment between  $|i\rangle \leftrightarrow |j\rangle$ ;  $\epsilon_0$  is the permittivity of vacuum; and  $E_f$  ( $f = s, c, p$ ) is the electric-field amplitude of  $E_f$ . Given that  $n = \sqrt{1 + \chi} \approx 1 + \chi/2$ ,  $\chi = \chi' + i\chi''$ , and  $n = n_0 + n_R + in_I$  ( $n_0 = 1$  is the background index of the atomic medium), the real and imaginary parts of the refractive index can be written as  $n_R \approx \chi'/2 = N\mu_{13}/(\epsilon_0 E_s) \times \text{Re}(\rho_{31})$  and  $n_I \approx \chi''/2 = N\mu_{13}/(\epsilon_0 E_s) \times \text{Im}(\rho_{31})$ . To achieve the PT-symmetric condition in the current setting, the imaginary part  $\text{Im}(\rho_{31})$  should be negative (gain) and positive (loss) in the corresponding four-level configurations, while the real part  $\text{Re}(\rho_{31})$  should be the same (symmetric). By making use of the advantage of this multi-parameter tunable system, in which the loss and gain can be independently adjusted by the parameters (mainly the Rabi frequency  $\Omega_f$ ) of the signal and pump beams, we can construct the desired refractive index profile satisfying  $n(x) = n^*(-x)$  as shown in Figure 2. Here the frequency detunings for the signal, coupling, and pump fields are defined as  $\Delta_s = \omega_{31} - \omega_s$ ,  $\Delta_c = \omega_{32} - \omega_c$ , and  $\Delta_p = \omega_{41} - \omega_p$ , respectively.

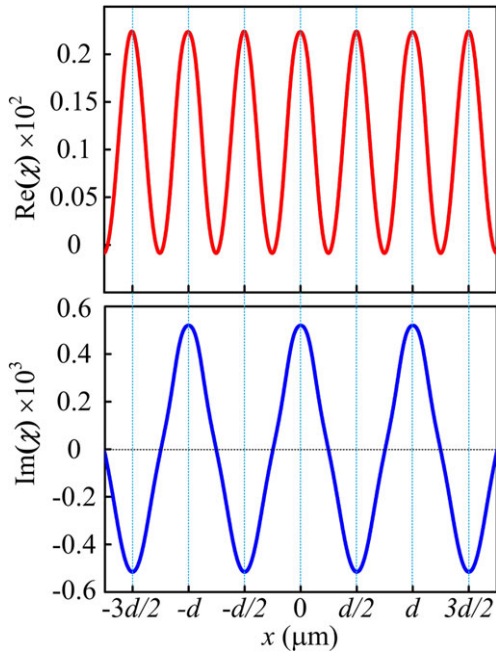


**Figure 2.** a) Real and b) imaginary parts of the refractive index for the signal field as a function of position  $x$  when the intensities of the signal field and the pump field are both spatially modified.  $\Omega_c = 2\pi \times 2.2$  MHz,  $\Omega_s = 2\pi \times [7.5 + 3\cos(\pi x/2)]$  MHz,  $\Omega_p = 2\pi \times 5.1 \times [1 + \cos(\pi x/2)]$  MHz,  $\Delta_p = 58.2$  MHz,  $\Delta_c = -85.626$  MHz, and  $\Delta_s = -2\pi \times 15.16$  MHz.  $d$  is the periodicity of the signal and pump fields. The intensity of the pump field at positions  $-d$ ,  $0$ , and  $d$  is zero.

#### 4. Results and Analysis

**Figure 3** depicts the detected signal field on the CCD camera under different conditions. First, with the frequency detuning of the signal field tuned far away from the atomic resonance, one sees the simple interference fringes of  $E_s$  and  $E'_s$  in Figure 3a. As the signal frequency is tuned to be near resonant with the transition  $|1\rangle \leftrightarrow |3\rangle$ , it is dramatically absorbed (Figure 3b). When the large Gaussian coupling field  $E_c$  is turned on, it induces EIT on the signal field and reduces its absorption (Figure 3c) under the two-photon resonance satisfying  $\Delta_s - \Delta_c = 0$ . The amount of residual absorption is determined by the coupling beam parameters. Then, by injecting the standing-wave pump field shown in Figure 3d into the cell, alternative gain and loss channels with a controllable contrast are obtained on the signal field by carefully arranging the coupling- and pump-field parameters. Inside the cell, the two standing-wave fields with the same period completely overlap with each other. The presence of the pump field (with enough intensity) can couple a four-level  $N$ -type system and therefore can lead to a gain on the signal field.<sup>[42]</sup> Notice that the intensity of the pump field at the dark-fringe channels is weak and almost zero at the exact valley, which indicates that a controllable loss exists in dark-fringe channels. As shown in Figure 3e, one can clearly find the alternate gain (bright fringes with strong pump field) and loss (dark fringes with weak/no pump field) in the middle region of the periodic field by comparing it with the original intensity profile of the signal field shown in Figure 3a. Figure 3f shows the transmission spectra of the signal field under different conditions from another auxiliary Rb cell for calibrating the detuning of the lasers.

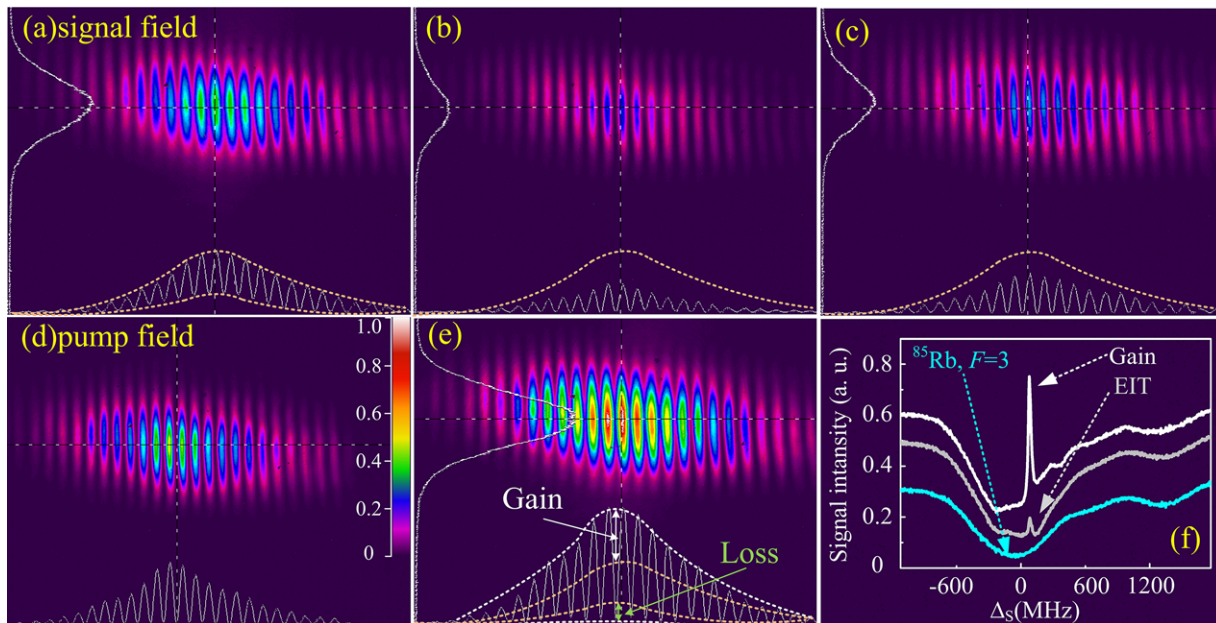


**Figure 3.** a) Observed image and intensity profiles of the signal field  $E_s$  without interacting with atoms. b) Signal field after propagating through the atomic medium under the resonant condition (simple atomic absorption). c) Reduced absorption with the generated EIT when the Gaussian coupling field  $E_c$  is turned on. d) The standing-wave pump field. e) Alternating gain and loss profiles on  $E_s$  with both  $E_c$  and pump field  $E_p$  turned on. (a–e) share the same color bar as (d). The units of the color bar are mW. f) Reference spectra of the signal field in the frequency domain. The middle and lower curves are the observed EIT signal and the absorption spectrum corresponding to the transition of  $^{85}\text{Rb}$ ,  $F = 3 \rightarrow F'$ , respectively. The upper curve with a high peak represents the Raman gain.



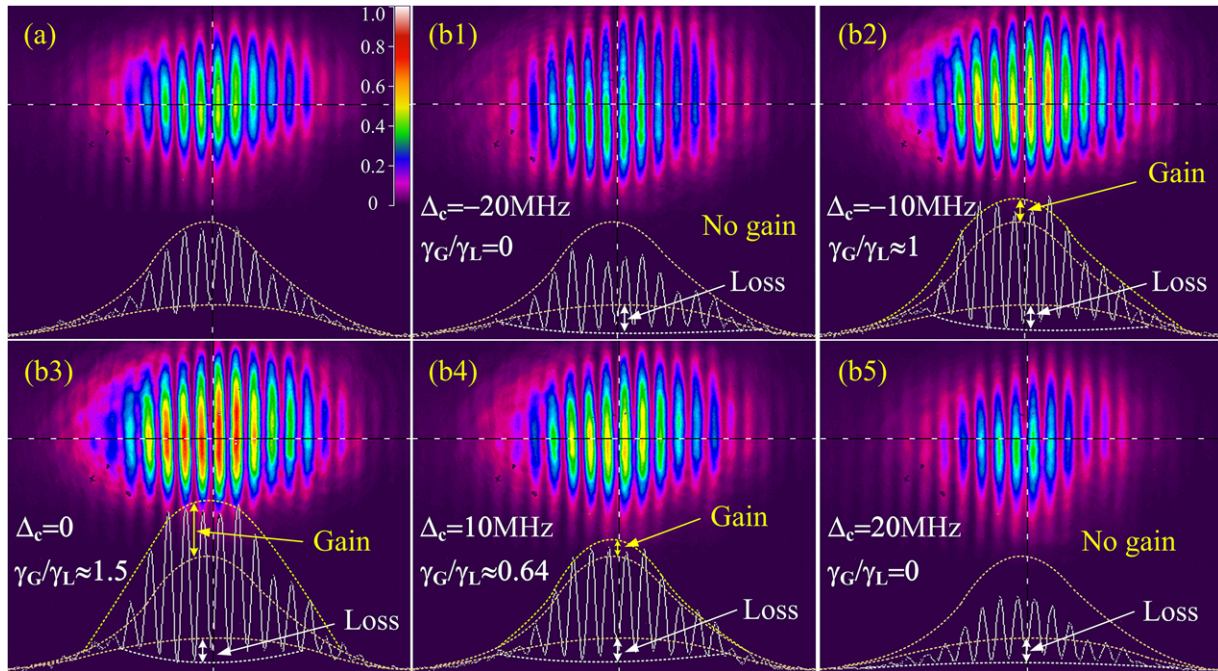


**Figure 4.** a) The initial intensity profile of  $E_s$  without absorption. b1–b5) Typical evolution of the gain/loss ( $\gamma_G/\gamma_L$ ) ratio versus the coupling frequency detuning  $\Delta_c$ . All the pictures share the same color bar as (a). The units of the color bar are mW.

By taking advantage of the atomic coherence, the ratio between the induced gain and loss can be easily controlled by carefully adjusting the experimental parameters. The ratio  $\gamma_G/\gamma_L$  ( $\gamma_G$  and  $\gamma_L$  representing the gain and loss coefficients, respectively) for describing the non-Hermitian system can be directly measured from the generated gain and loss components. In the current atomic configuration, the intensity for the detected signal field can be written as  $I = I_0 - I_0 e^{-aL} \approx I_0 - I_0(1 - aL)$ , where  $a = (2\pi/\lambda_s)\chi''$ , and  $I_0$  is defined as the initial intensity of the signal field and  $L$  as the cell length. The loss or gain is determined by the sign of  $\chi''$ , namely, the negative (positive)  $n_1$  represents the gain (loss). Consequently, we have  $I \propto \chi'' = 2n_1$ , which means that the ratio between the observed gain and loss intensities can be equivalent to the ratio  $\gamma_G/\gamma_L$ . **Figure 4a** gives the original intensity profile of the standing-wave signal field, and **Figure 4b1–b5** shows the typical evolution of the ratio  $\gamma_G/\gamma_L$  versus the detuning  $\Delta_c$  of the coupling field with the signal-field detuning tuned to be near resonant with the transition  $5S_{1/2}, F = 3 \rightarrow 5P_{1/2}, F = 3$  of  $^{85}\text{Rb}$ . As the detuning  $\Delta_c$  is tuned from the far detuned points ( $\Delta_c = \pm 20$  MHz) to the resonant point ( $\Delta_c = 0$ ), the gain can be greatly enhanced, which can be attributed to the better satisfying of the two-photon resonant condition  $\Delta_s - \Delta_c = 0$ .

The results in **Figure 4** show that the ratio  $\gamma_G/\gamma_L$  can be in the range of 0–1.5, covering the required condition of  $\gamma_G/\gamma_L = 1$  (balanced gain and loss) for exact PT symmetry. Actually, even for an unbalanced gain–loss case (namely,  $\gamma_G \neq \gamma_L$ ), it can be mathematically transformed into an exact PT-symmetric one ( $\gamma_G = \gamma_L$ ) by using the gauge transformation<sup>[6]</sup> in Wick space, and be understood as “quasi-PT symmetry.”<sup>[43]</sup> A quasi-PT-symmetric Hamiltonian possesses a characteristic eigenvalue pattern with a new offset center instead of the original zero point (for the balanced case), and can present the same (below threshold) or

similar (above threshold) dynamic behaviors to its PT-symmetric counterpart.<sup>[44]</sup> Consequently, an unbalanced gain–loss case can also demonstrate the dynamic behaviors similar to the exactly balanced case.

The dynamic behaviors of the established non-Hermitian system below and above the symmetry breaking threshold are demonstrated by the relative phase difference  $\nu$  between two neighbouring gain and loss channels. A reference beam from the same laser as the signal beam is introduced to interfere with the generated gain–loss lattice, and the reference pattern looks like a 2D lattice with bright (in gain channels) and dark (in loss channels) squares. **Figure 5a** shows the case without gain, namely, the phase difference is  $\nu = 0$ . In **Figure 5a**, two black solid lines are added to mark the center of two adjacent fringes along the  $\gamma$  direction, and the distance between them is defined as  $2\pi$ . The distance mentioned in the current work is along the  $\gamma$  direction. The black dashed line indicates the middle between the two solid lines and just marks the center of the dark square in the case of no gain. Consequently, the distance between the marked bright square (indicated by the upper black solid line) and dark square is  $\pi$ . With the gain introduced, the relative distance between the dark and bright regions will be modified by changing the gain/loss ratio.

As shown in **Figure 5b–e**, the relative phase difference increases from  $0.16\pi$  to  $\pi$  with the gain/loss ratio adjusted from 0.1 to 1. The phase difference is obtained by measuring the relative distance between the black and white dashed lines. The added white dashed line represents the center of the shifted dark square. By comparing the measured distance with the reference length (in unit of  $\pi$ ) as defined in **Figure 5a**, one can determine the value of the phase difference. This phase difference directly reflects the internal phase difference of the eigenvectors in a

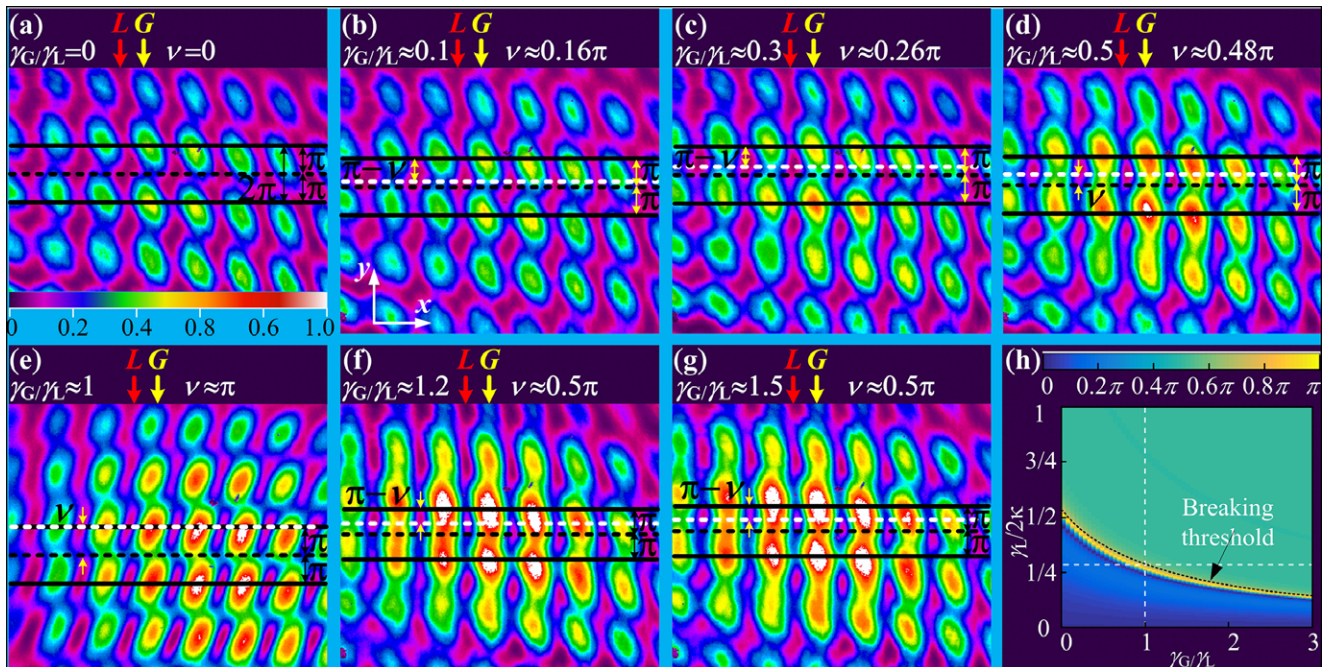


**Figure 5.** Measured phase difference between two neighboring gain and loss channels, which are marked by **G** and **L**, respectively. a) The phase difference  $\nu = 0$  for the case without gain. The double-sided arrow between the two black solid lines marks the distance between two adjacent fringes along the  $y$  direction and its length is defined as  $2\pi$ . b–e) The measured  $\nu$  at different gain/loss ratios for the cases below the PT-symmetry breaking threshold. The white dashed line marks the center of one dark square in the loss channel, and the distance between the white and black dashed lines represents the relative phase difference  $\nu$  between the gain and loss channels. f–g) The measured  $\nu$  is fixed at  $\pi/2$  when PT symmetry is broken. (b–g) share the same color bar as (a). The units of the color bar are mW. The reference beam keeps unchanged for every picture. h) The simulated phase difference with 10 gain–loss channels coupled. Term  $\kappa$  is the coupling coefficient between two adjacent gain and loss channels.

PT-symmetric system, while the eigenvalues are the basic criteria to determine whether the system is operating below or above the symmetry breaking threshold.<sup>[3,6]</sup> Theoretically, the corresponding phase difference below and above such threshold should be different.<sup>[6]</sup> For the case below the phase-transition point, the relative phase differences  $\nu$  can increase (from the initial values 0) with the gain/loss ratio. For the cases at and above the phase-transition point, the phase differences remain at  $\pi/2$  even with further increase of the gain. The phase information for above PT-symmetry breaking point is given at points  $\gamma_G/\gamma_L = 1.2$  and 1.5, as shown in Figure 5f,g, respectively. Actually, when the ratio  $\gamma_G/\gamma_L$  is increased to 1.2, the phase difference jumps from  $\pi$  ( $\gamma_G/\gamma_L = 1$ ) to  $\nu = \pi/2$ . When the ratio further increases to  $\gamma_G/\gamma_L = 1.5$ , the measured phase difference remains at  $\pi/2$ .

Figure 5h theoretically predicts the evolution of the phase difference in a PT-symmetric lattice with ten coupled gain–loss channels. The dynamical behaviors of the system is calculated based on the paraxial wave equation  $i\partial E/\partial z + \partial^2 E/\partial x^2 + V(x)E = 0$ , where  $V(x)$  is the potential of the periodic gain–loss structure and  $E$  is the electric field envelope in each channel.<sup>[3,6,28,34]</sup> The results from this theoretical simulation can well explain our experimentally observed phase difference jump across the threshold point. Particularly, for the points below but very close to the threshold, the phase difference is predicted to take the  $\pi$  value in a very small range, which is also confirmed by the experiment.

## 5. Conclusion

In summary, PT-symmetric optical lattice with a controllable gain/loss ratio and the phase transition at the symmetry breaking threshold are experimentally demonstrated based on four-level atomic configurations excited by spatially alternating strong and weak pump fields in the same <sup>85</sup>Rb atomic medium. The gain–loss profiles are generated by the active Raman gain and modified (EIT) absorption due to laser-induced atomic coherence effects. Compared to the previous work based on discrete diffraction for the signal field,<sup>[34,45]</sup> the current scheme is much easier to operate in real experiment. More importantly, the gain and loss coefficients can be adjusted more independently, which will be easier to control the gain, loss, and coupling coefficients to realize the PT-symmetric condition and study related effects. Furthermore, by taking advantage of the large parametric space in multi-level atomic configurations, such newly demonstrated periodic gain/loss optical lattices can provide a more flexible platform to investigate the diverse effects such as solitons in PT-symmetric nonlinear lattices<sup>[46]</sup> and unidirectional light transport<sup>[47]</sup> resulting from the interplay between non-Hermitian Hamiltonian and nonlinear effects,<sup>[48,49]</sup> and various beam dynamical properties such as non-Hermitian Bloch oscillation<sup>[17,18]</sup> predicted in non-Hermitian optical lattices. Also, this EIT-based scheme can be extended to various atom-like solid materials, and hopefully create useful PT-symmetric optical devices.



## Acknowledgements

This work was supported in part by National Key R&D Program of China (2017YFA0303703, 2018YFA0307500), National Natural Science Foundation of China (61605154, 11474228), Natural Science Foundation of Shaanxi Province (2017JQ6039, 2017JZ019), Postdoctoral Science Foundation of Shaanxi Province (2017BSHYDZZ54, 2017BSHTDZZ18), and China Postdoctoral Science Foundation (2016M600776, 2016M600777, 2017T100734). L.Y. is sponsored by Fundamental Research Funds for the Central Universities (HEUCFJ170402).

## Conflict of Interest

The authors declare no conflict of interest.

## Keywords

atomic coherence, optical lattice, parity-time symmetry

Received: June 3, 2018

Revised: July 10, 2018

Published online:

- [1] G. Lévai, M. Znojil, *J. Phys. Math. Gen.* **2000**, *33*, 7165.
- [2] C. M. Bender, *Rep. Prog. Phys.* **2007**, *70*, 947.
- [3] R. El-Ganainy, K. G. Makris, D. N. Christodoulides, Z. H. Musslimani, *Opt. Lett.* **2007**, *32*, 2632.
- [4] S. Klaiman, U. Günther, N. Moiseyev, *Phys. Rev. Lett.* **2008**, *101*, 080402.
- [5] D. N. Christodoulides, M. A. Miri, *Proc. SPIE* **2014**, *9162*, 91621P.
- [6] C. E. Ruter, K. G. Makris, R. El-Ganainy, D. N. Christodoulides, M. Segev, D. Kip, *Nat. Phys.* **2010**, *6*, 192.
- [7] Y. D. Chong, L. Ge, H. Cao, A. D. Stone, *Phys. Rev. Lett.* **2010**, *105*, 053901.
- [8] B. Peng, S. K. Özdemir, F. Lei, F. Monifi, M. Gianfreda, G. L. Long, S. Fan, F. Nori, C. M. Bender, L. Yang, *Nat. Phys.* **2014**, *10*, 394.
- [9] L. Chang, X. Jiang, S. Hua, C. Yang, J. Wen, L. Jiang, G. Li, G. Wang, M. Xiao, *Nat. Photon.* **2014**, *8*, 524.
- [10] R. El-Ganainy, K. G. Makris, M. Khajavikhan, Z. H. Musslimani, S. Rotter, D. N. Christodoulides, *Nat. Phys.* **2018**, *14*, 116.
- [11] L. Feng, R. El-Ganainy, L. Ge, *Nat. Photon.* **2017**, *11*, 752.
- [12] T. Goldzak, A. A. Mailybaev, N. Moiseyev, *Phys. Rev. Lett.* **2018**, *120*, 013901.
- [13] W. Wang, L. Wang, R. Xue, H. Chen, R. Guo, Y. Liu, J. Chen, *Phys. Rev. Lett.* **2017**, *119*, 077401.
- [14] K. G. Makris, R. El-Ganainy, D. N. Christodoulides, Z. H. Musslimani, *Phys. Rev. A* **2010**, *81*, 063807.
- [15] Z. H. Musslimani, K. G. Makris, R. El-Ganainy, D. N. Christodoulides, *Phys. Rev. Lett.* **2008**, *100*, 030402.
- [16] M. Wimmer, A. Regensburger, M.-A. Miri, C. Bersch, D. N. Christodoulides, U. Peschel, *Nat. Commun.* **2015**, *6*, 7782.
- [17] S. Longhi, *Phys. Rev. Lett.* **2009**, *103*, 123601.
- [18] M. Wimmer, M. A. Miri, D. N. Christodoulides, U. Peschel, *Sci. Rep.* **2015**, *5*, 17760.
- [19] X. B. Yin, X. Zhang, *Nat. Mater.* **2013**, *12*, 175.
- [20] Z. Lin, H. Ramezani, T. Eichelkraut, T. Kottos, H. Cao, D. N. Christodoulides, *Phys. Rev. Lett.* **2011**, *106*, 213901.
- [21] A. Regensburger, C. Bersch, M. A. Miri, G. Onishchukov, D. N. Christodoulides, U. Peschel, *Nature* **2012**, *488*, 167.
- [22] T. Eichelkraut, R. Heilmann, S. Weimann, S. Stützer, F. Dreisow, D. N. Christodoulides, S. Nolte, A. Szameit, *Nat. Commun.* **2013**, *4*, 2533.
- [23] J. H. Wu, M. Artoni, G. C. La Rocca, *Phys. Rev. A* **2015**, *91*, 033811.
- [24] M. A. Miri, A. Regensburger, U. Peschel, D. N. Christodoulides, *Phys. Rev. A* **2012**, *86*, 023807.
- [25] H. Ramezani, D. N. Christodoulides, V. Kovanis, I. Vitebskiy, T. Kottos, *Phys. Rev. Lett.* **2012**, *109*, 033902.
- [26] O. Bendix, R. Fleischmann, T. Kottos, B. Shapiro, *Phys. Rev. Lett.* **2009**, *103*, 030402.
- [27] A. Regensburger, M. A. Miri, C. Bersch, J. Näger, G. Onishchukov, D. N. Christodoulides, U. Peschel, *Phys. Rev. Lett.* **2013**, *110*, 223902.
- [28] K. G. Makris, R. El-Ganainy, D. N. Christodoulides, Z. H. Musslimani, *Phys. Rev. Lett.* **2008**, *100*, 103904.
- [29] M. C. Zheng, D. N. Christodoulides, R. Fleischmann, T. Kottos, *Phys. Rev. A* **2010**, *82*, 010103(R).
- [30] J. H. Wu, M. Artoni, G. C. La Rocca, *Phys. Rev. Lett.* **2014**, *113*, 123004.
- [31] J. T. Sheng, M. A. Miri, D. N. Christodoulides, M. Xiao, *Phys. Rev. A* **2013**, *88*, 041803(R).
- [32] C. Hang, Y. V. Kartashov, G. Huang, V. V. Konotop, *Opt. Lett.* **2015**, *40*, 2758.
- [33] M. Chitsazi, H. Li, F. M. Ellis, T. Kottos, *Phys. Rev. Lett.* **2017**, *119*, 093901.
- [34] Z. Zhang, Y. Zhang, J. Sheng, L. Yang, M. Miri, D. N. Christodoulides, B. He, Y. Zhang, M. Xiao, *Phys. Rev. Lett.* **2016**, *117*, 123601.
- [35] S. A. R. Horsley, M. Artoni, G. C. La Rocca, *Nat. Photon.* **2015**, *9*, 436.
- [36] M. O. Scully, *Phys. Rev. Lett.* **1991**, *67*, 1855.
- [37] Z. Zhang, D. Ma, J. Sheng, Y. Zhang, Y. Zhang, M. Xiao, *J. Phys. B At. Mol. Opt. Phys.* **2018**, *51*, 072001.
- [38] S. E. Harris, *Phys. Today* **1997**, *50*, 36.
- [39] J. Gea-Banacloche, Y. Q. Li, S. Z. Jin, M. Xiao, *Phys. Rev. A* **1995**, *51*, 576.
- [40] M. Xiao, Y. Li, S. Jin, J. Gea-Banacloche, *Phys. Rev. Lett.* **1995**, *74*, 666.
- [41] Z. Zhang, J. Feng, X. Liu, J. Sheng, Y. Zhang, Y. Zhang, Min Xiao, *Opt. Lett.* **2018**, *43*, 919.
- [42] H. S. Kang, L. L. Wen, Y. F. Zhu, *Phys. Rev. A* **2003**, *68*, 063806.
- [43] O. Marco, S. Alexander, *J. Opt.* **2014**, *16*, 065501.
- [44] A. Lupu, H. Benisty, A. Degiron, *Opt. Express* **2013**, *21*, 21651.
- [45] Z. Y. Zhang, X. Liu, D. Zhang, J. T. Sheng, Y. Q. Zhang, Y. P. Zhang, M. Xiao, *Phys. Rev. A* **2018**, *97*, 013603.
- [46] F. K. Abdullaev, Y. V. Kartashov, V. V. Konotop, D. A. Zezyulin, *Phys. Rev. A* **2011**, *83*, 041805(R).
- [47] H. Ramezani, T. Kottos, R. El-Ganainy, D. N. Christodoulides, *Phys. Rev. A* **2010**, *82*, 043803.
- [48] V. V. Konotop, J. Yang, D. A. Zezyulin, *Rev. Mod. Phys.* **2016**, *88*, 035002.
- [49] S. V. Suchkov, A. A. Sukhorukov, J. Huang, S. V. Dmitriev, C. Lee, Y. S. Kivshar, *Laser Photon. Rev.* **2016**, *10*, 177.